Nano Research 2015, 8(3): 751–764
DOI 10.1007/s12274-014-0558-0
Research Article

ISSN 1998-0124
CN 11-5974/O4

Mesoporous silica nanorods intrinsically doped with photosensitizers as a multifunctional drug carrier for combination therapy of cancer

Guangbao Yang, Hua Gong, Xiaoxin Qian, Pengli Tan, Zhiwei Li, Teng Liu, Jingjing Liu, Youyong Li (✉), and Zhuang Liu (✉)

Institute of Functional Nano and Soft Materials (FUNSOM), Collaborative Innovation Center of Suzhou Nano Science and Technology, Soochow University, Suzhou, Jiangsu 215123, China

Received: 23 May 2014
Revised: 8 August 2014
Accepted: 9 August 2014

KEYWORDS
mesoporous silica nanorods,
chlorin e6,
photodynamic therapy,
drug delivery,
combination therapy

ABSTRACT

Mesoporous silica nanoparticles (MSNs) have attracted tremendous attention in recent years as drug delivery carriers due to their large surface areas, tunable sizes, facile modification and considerable biocompatibility. In this work, we fabricate an interesting type of MSNs which are intrinsically doped with photosensitizing molecules, chlorin e6 (Ce6). By increasing the amount of Ce6 doped inside the silica matrix, it is found that the morphology of MSNs changes from spheres to rod-like shapes. The obtained Ce6-doped mesoporous silica nanorods (CMSNRs) are not only able to produce singlet oxygen for photodynamic therapy, but can also serve as a drug delivery platform with high drug loading capacity by utilizing their mesoporous structure. Compared to spherical nanoparticles, it is found that CMSNRs with a larger aspect ratio show much faster uptake by cancer cells. With doxorubicin (DOX) employed as a model drug, the combined photodynamic and chemotherapy is carried out, achieving synergistic anti-tumor effects both *in vitro* and *in vivo*. Our study presents a new design of an MSN-based drug delivery platform, which intrinsically is fluorescent and able to serve as a photodynamic agent, promising for future imaging-guided combination therapy of cancer.

1 Introduction

In the past decade, various silica-based nanostructures have been synthesized and shown great potential in many fields including biomedicine [1–8]. Owing to their easy synthesis, tunable size and morphology [9, 10], and good biocompatibility, those fabricated silica nanostructures, particularly mesoporous silica nanoparticles (MSNs), have been intensively explored for applications ranging from bioimaging [11–15] to

Address correspondence to Zhuang Liu, zliu@suda.edu.cn; Youyong Li, yyli@suda.edu.cn

drug [16–21] and gene delivery [22, 23]. Photodynamic therapy (PDT) is a non-invasive therapeutic method in which cancer cells or other lesions are damaged by a combination of light and photosensitizers (PS) in the presence of oxygen [24–28]. Without light exposure, PS molecules are largely nontoxic to cells [29], thus offering much reduced side effects compared to traditional chemotherapy or radiotherapy. To date, abundant studies have demonstrated that MSNs can be loaded with various anticancer drugs (e.g., doxorubicin) and photosensitizers via hydrophobic interactions for delivery of chemotherapy and PDT, respectively [30–35]. However, when physically adsorbed into the mesoporous structures of MSNs, the PS molecules may be prematurely released from the carrier, leading to a reduced efficiency of treatment and as well as potential side-effects [36].

Covalent doping of PS molecules inside nanoparticles is expected to overcome these drawbacks. In recent work by Ishimura et al., a novel type of silica/tetrakis(4-carboxyphenyl)porphyrin (TCPP) hybrid nanoring was synthesized by a one-pot sol–gel reaction using a TCPP-conjugated silica precursor, and used for fluorescence imaging of tumors [37]. Similar strategies have also been reported in several other studies to fabricate silica nanoparticles with porphyrin derivatives doped inside the silica matrix for either fluorescent imaging or *in vitro* photodynamic therapy [38–41]. The *in vivo* therapeutic use of those nanostructures, however, has not yet been demonstrated thus far. More importantly, there is much room to utilize those mesoporous nanostructures with intrinsically doped PS molecules as a multifunctional drug carrier for combination therapy of cancer (e.g., combined photodynamic and chemotherapy).

In this work, chlorin e6 (Ce6), a widely used PS molecule, is doped inside the silica matrix of mesoporous silica nanostructures. It was found that the shape of as-synthesized nanostructures could be precisely controlled by the feeding amount of Ce6, and an increase in the amount of Ce6 led to a morphology change of the nanostructures from spheres into rods. Interestingly, compared with spherical mesoporous silica nanoparticles (MSNP), Ce6-doped mesoporous silica nanorods (CMSNRs) with higher aspect ratios show increased uptake by cancer cells. Taking advantage of their mesoporous structure, these CMSNRs are then utilized as a drug carrier for intracellular delivery of doxorubicin (DOX), a chemotherapeutic drug. Combined photodynamic therapy and chemotherapy, relying on Ce6 doped inside the silica matrix and DOX loaded into the mesoporous silica structure, respectively, is then achieved both *in vitro* and *in vivo* using CMSNRs loaded with DOX (CMSNRs/DOX). In our animal experiments, in particular, an obvious synergistic tumor growth inhibition effect was observed by such combination therapy, which furthermore results in no noticeable toxicity to the treated animals.

2 Experimental

2.1 Materials

Cetyltrimethylammouium bromide (CTAB), aqueous ammonia ($NH_3{\cdot}H_2O$), dimethylsulfoxide (DMSO), and ammonium nitrate (NH_4NO_3) were purchased from Sinopharm Chemical Reagent Co. Tetraethyl orthosilicate (TEOS), 3-aminopropyltriethoxysilane (APTES), 1-ethyl-3-(3-dimethylaminopropyl) carbodiimide hydrochloride (EDC-HCl), and *N*-hydroxysuccinimide (NHS) were obtained from Sigma Aldrich. Ce6 was the product of J&K Chemical Co. DOX was bought from Beijing HuaFeng United Technology Co. Ltd. All chemicals were used as purchased without further purification.

2.2 Synthesis and characterization of CMSNRs

To synthesize CMSNRs, we first conjugated Ce6 with APTES by mixing 2.2 mg of Ce6 pre-dissolved in 0.5 mL of DMSO with 12 μL of APTES, 6 mg of EDC-HCl, and 4 mg of NHS. The mixture was stirred for 2 h at room temperature and then added into 10 mL water containing 528 μL $NH_3{\cdot}H_2O$ (28%–30%) and 11.2 mg of CTAB under magnetic stirring. Finally, 58 μL of TEOS was added dropwise into the reaction solution, which was stirred for 24 h at 50 °C before the product was collected by centrifugation. The shape and size of CMSNRs were controlled by changing the amount of added Ce6–APTES while maintaining the concentrations of CTAB and TEOS. The obtained CMSNRs were collected by centrifugation at 14,800 rpm for

5 min, washed with ethanol three times and then dispersed in 20 mL of ethanol containing 240 mg of NH_4NO_3. The mixture was heated to 45 °C under stirring for 6 h in order to remove the surfactant template. The final products were washed with ethanol for three times and then dispersed in water for future use.

The morphology of CMSNRs was characterized by using a Philips CM300 transmission electron microscope (TEM). UV–Vis spectra were carried out using PerkinElmer Lambda 750 UV/Vis/NIR spectrophotometer. Fluorescence spectra of CMSNRs4/DOX were obtained using a FluoroMax 4 luminescence spectrometer (HORIBA Jobin Yvon). The concentration of Ce6 loaded on CMSNRs was determined by the Ce6 characteristic absorption peak at 404 nm with a molar extinction coefficient of 1.1×10^5 $M^{-1}\cdot cm^{-1}$ after subtracting the absorbance contributed by MSNs at the same wavelength.

2.3 Drug loading and release

For DOX loading, 2.0 mg of CMSNRs4 were mixed with different concentrations of DOX in 4 mL of phosphate buffered saline (PBS) (pH = 8.0), and stirred at room temperature for 24 h. Excess unbound DOX was removed by centrifugation at 14,800 rpm for 5 min and repeated water washing. The amount of DOX loaded in the CMSNRs4 was measured by UV–Vis spectroscopy. The obtained samples were stored under 4 °C until use. To study the drug release, a solution of CMSNRs4/DOX was dialyzed against PBS with different pH values (7.4 or 5.5) at room temperature. The amounts of DOX and Ce6 released into the dialysis media at different time points were measured by UV–Vis spectroscopy.

2.4 Detection of singlet oxygen

In our experiments, we used the light source in the Maestro *in vivo* animal imaging system to trigger PDT. Different samples were exposed to light with a central wavelength at 660 nm. The power density was measured by an optical power meter (LPE-1C, Physcience Opto-Electronics, Beijing) to be 5 mW/cm^2. A singlet oxygen sensor green (SOSG), which is highly sensitive for singlet oxygen, was employed here during the detection process. Typically, SOSG at a concentration of 2.5 μM was incubated with nanoparticles for 10 min before light irradiation and SO generation measurement. The tested samples included free Ce6, MSNs without Ce6 loading, and CMSNRs4. The generated SO was determined by measuring the recovered SOSG fluorescence under 494-nm excitation.

2.5 Cellular experiments

4T1, HeLa, and 293T cells were originally obtained from American Type Culture Collection (ATCC) and cultured in the recommended medium at 37 °C in a 5% CO_2 atmosphere. For cell toxicity assay, cells were seeded into 96-well plates (1×10^4 per well) until adherent and then incubated with series concentrations of MSNs, free Ce6, and CMSNRs4. After incubation for 24 h, the standard thiazolyl tetrazolium (MTT, Sigma-Aldrich) test was conducted to measure the cell viabilities relative to the untreated cells.

For photodynamic therapy, 4T1 cells seeded in 96-well plates were mixed with CMSNRs4 and free Ce6 at various concentrations. After 12 h, the cells were exposed to 660-nm irradiation at a power density of 5 mW/cm^2 for 1 h. Cells were transferred into fresh media and further incubated for 24 h. The standard MTT test was then conducted to measure the relative cell viabilities. For chemotherapy, 4T1 cells were seeded into 96-well plates until adherent and then incubated with CMSNRs4/DOX and free DOX for 36 h before the MTT test. For combination therapy, 4T1 cells pre-seeded in 96-well plates were incubated with series of concentrations of CMSNRs4 or CMSNRs4/DOX for 12 h and then treated with or without 660-nm light exposure (5 mW/cm^2 for 1 h). The cells were then transferred into fresh media and re-incubated at 37 °C for an additional 24 h before MTT assay to determine the relative cell viabilities. The cell viabilities resulting from the theoretical additive effect were determined by multiplying the remaining relative cell viabilities after two monotherapies. A similar approach was applied to calculate the theoretical additive effect for *in vivo* experiment (final tumor volumes).

For confocal fluorescence imaging, 4T1 cells (1×10^5 cells) were cultured in 24-well plates containing 100 μg/mL CMSNRs4/DOX in the dark for different

periods of time (0.5, 1, 2, 6, and 10 h). After washing three times with PBS (pH = 7.4), cells were labeled with 4′, 6-diamidino-2-phenylindole (DAPI) and then imaged by a laser scanning confocal fluorescence microscope (Leica SP5).

To determine the cell uptake of CMSNRs with various aspect ratios, 4T1 cells (5×10^6 cells) were cultured in 24-well plates containing CMSNRs1, CMSNR2, CMSNRs3, and CMSNRs4 with the same concentrations of silica (100 μg/mL) for different incubation times (1, 2, 3, and 6 h). After washing three times with PBS (pH = 7.4), the cells were treated using cell lysis solution (2% sodium dodecyl sulfonate). The obtained solution was transferred into a solution containing 6 mL of HCl, 2 mL of HNO_3, 2 mL of $HClO_4$, and 100 μL of HF. The mixture was heated at 100 ℃ for about 2 h to yield a colorless solution, which was diluted to 10 mL by deionized water. The concentration of Si was measured by inductively coupled plasma–atomic emission spectrometry (ICP–AES).

2.6 *In vivo* experiments

Female Balb/c mice weighing 18–20 g were purchased from Nanjing Peng Sheng Biological Technology Co. Ltd. and used in accordance with regulations provided by Soochow University Laboratory Animal Center. 4T1 tumors were inoculated by subcutaneous injection of 5×10^6 cells in ~100 μL of serum-free RMPI-1640 medium onto the back of each mouse. After ~6 days, the mice bearing 4T1 tumors were treated when the tumor volume reached ~60 mm^3. 4T1 tumor-bearing mice were divided into 6 groups (n = 5 per group): (a) Untreated; (b) intratumorally (i.t.) injected with 50 μL CMSNRs4; (c) i.t. injected with 50 μL of CMSNRs4 and exposed to 660-nm light for 1 h; (d) i.t. injected with 50 μL of DOX + Ce6 and exposed to 660-nm light for 1 h; (e) i.t. injected with 50 μL of CMSNRs4/DOX; (f) i.t. injected with 50 μL CMSNRs4/DOX and exposed to 660-nm light for 1 h. Three days later, the PDT groups were given another dose of light exposure (with no further injection of other species). Tumor sizes were monitored every 2 days for 2 weeks. The lengths and widths of the tumors were measured by a digital caliper. The tumor volume was calculated according to the following formula: $\text{Width}^2 \times \text{length}/2$. Relative tumor volumes were calculated as V/V_0 (V_0 is the tumor volume when the treatment was initiated).

3 Results and discussion

The procedure for the synthesis of CMSNRs is illustrated in Fig. 1(a). Ce6 was covalently conjugated to APTES via the formation of amide bonds with the help of NHS and EDC-HCl. CMSNRs were then synthesized by co-condensation of TEOS together with different amounts of APTES-Ce6 in the presence of aqueous ammonia and CTAB. After purification to remove CTAB molecules in the porous structure by an ion-exchange method, water-dispersible CMSNRs were obtained and characterized by transmission electron microscopy (TEM) (Fig. 1(b) and S1 in the Electronic Supplementary Material (ESM)). Different from the spherical MSNPs prepared without addition of APTES-Ce6, the obtained CMSNRs showed different morphologies varying from spheres to rods. By increasing the feeding amount of APTES-Ce6 from 0.022 mg/mL to 0.154 mg/mL, we synthesized four types of rod-shaped CMSNRs with average dimensions of 208/170 nm (CMSNRs1), 307/108 nm (CMSNRs2), 311/90 nm (CMSNRs3), and 340/74 nm (CMSNRs4), which corresponded to aspect ratios of ~1.2, ~2.8, ~3.5, and ~4.6, respectively. A control experiment involving adding a simple mixture of APTES and Ce6 without EDC/NHS to induce cross-linking for nanoparticle fabrication demonstrated that Ce6 was indeed covalently conjugated to the silica matrix instead of being incorporated by non-covalent adsorption (Fig. S2, in the ESM).

The following model is proposed to explain the Ce6-concentration-dependent morphology change of the obtained CMSNRs (Fig. 1(c)). At a low concentration of Ce6, Ce6 molecules barely cover the seeding Si atoms (light green) on the edges of the nanostructure. Therefore TEOS could be connected onto different sides of the silica nanostructure (indicated by the four arrows in Fig. 1(c), left), leading to a more spherical shape of the obtained nanostructures. In contrast, at a high concentration of Ce6, Ce6 was able to cover the seeding Si atoms (dark green) on the edges of silica nanostructure. As a result of steric hindrance, TEOS is

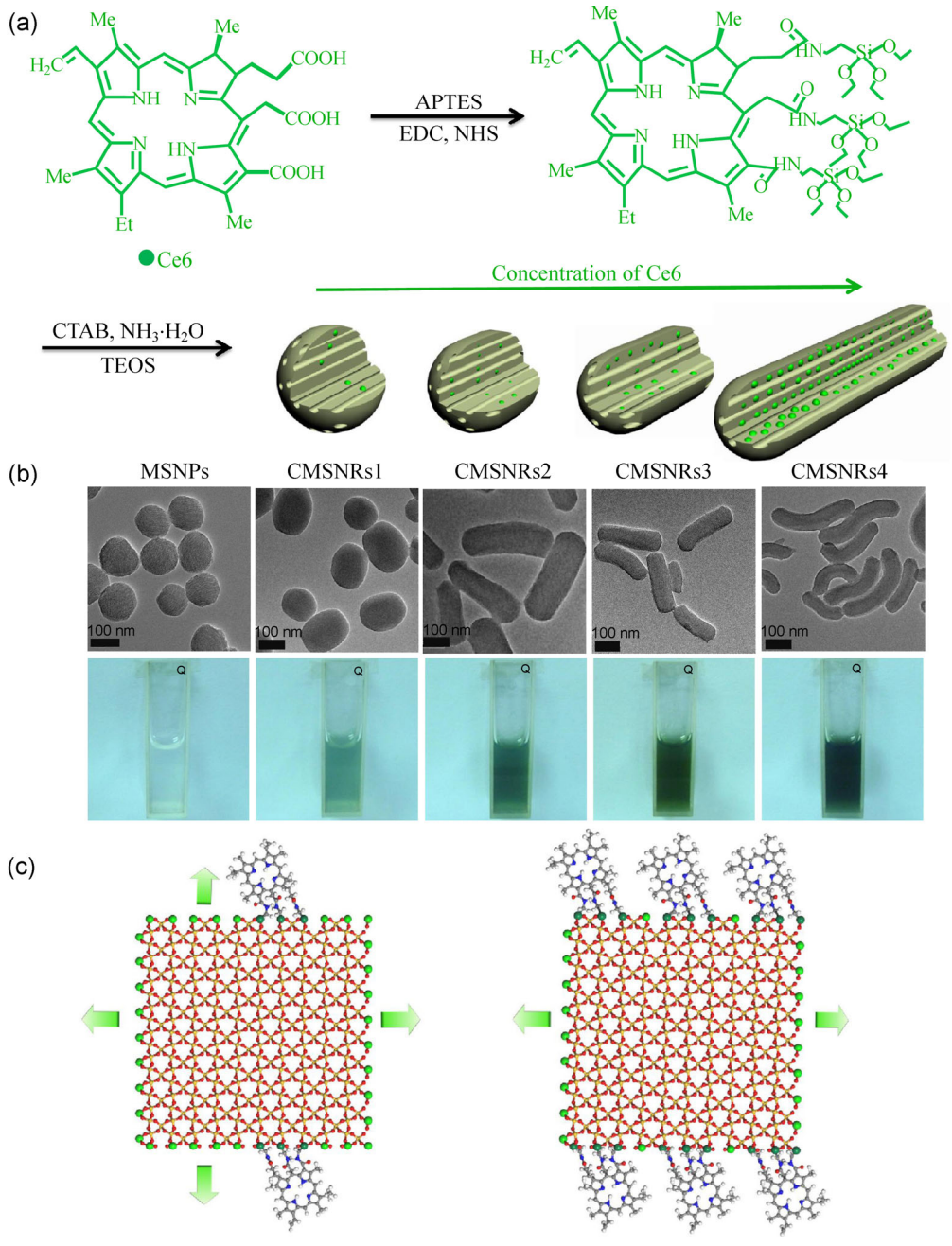

Figure 1 Synthesis of CMSNRs and theoretical model in the process of CMSNRs formation. (a) Synthetic process of Ce6-doped mesoporous silica nanorods (CMSNRs). (b) TEM images of CMSNRs (upper row) and their respective photographs in aqueous solutions (bottom row). These samples with different aspect ratios were prepared by adding increasing amount of Ce6. (c) The proposed theoretical model to explain Ce6 concentration-dependent morphology change of our synthesized CMSNRs. Left and right schemes represent silica nanostructures synthesized under low and high Ce6 concentrations, respectively.

thus be preferentially connected onto the exposed edges of the silica nanostructure (indicated by the two arrows in Fig. 1(c), right). Therefore, higher levels of Ce6 doping lead to rod-like shapes of the final silica nanostructures.

Successful Ce6 loading on MSNRs was evidenced by UV–Vis spectra of CMSNRs, in which the characteristic Ce6 absorption peaks were clearly identified (Fig. 2(a)). The UV–Vis peak at 404 nm was then used to determine the concentrations of Ce6 in CMSNRs samples after subtraction of the absorbance contributed by MSNs. With increasing Ce6 concentration, the

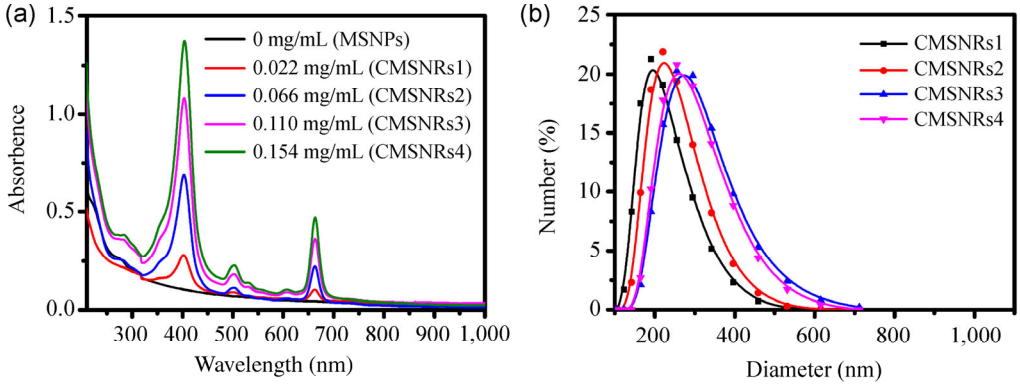

(c)

Samplcs	CMSNRs1	CMSNRs2	CMSNRs3	CMSNRs4
Aspect ratio	1.2	2.8	3.5	4.6
Ce6 loading (%)	1.225	3.738	6.09	7.51
BET ($m^2 \cdot g^{-1}$)	1,265	952	904	580
Pore size (nm)	2.9115	3.61	3.38	6.56

Figure 2 Characterization of CMSNRs. (a) UV–Vis–NIR spectra of MSNs and CMSNRs prepared at different feeding Ce6 concentrations. (b) Dynamic light scattering data of different CMSNRs. (c) Physicochemical characterization of CMSNRs obtained at different Ce6 feeding concentrations.

amount of Ce6 doped inside CMSNRs increased and approached a loading ratio of 7.51% (*w*/*w*) at a Ce6 feeding concentration of 0.154 mg/mL for CMSNRs4.

The average hydrodynamic sizes of the obtained CMSNRs were determined to be 200–300 nm as measured by dynamic light scattering (DLS), suggesting that these nanorods were well dispersed in the aqueous solution without significant aggregation (Fig. 2(b)). Brunauer–Emmett–Teller (BET) surface area and pore volume measurements were carried out for those CMSNRs samples. The pore sizes of CMSNRs1, CMSNRs2, and CMSNRs3 were found to be similar, while that of CMSNRs4 appeared to be larger than in the former three types of CMSNRs. However, with the increase of Ce6 doping, the surface area of CMSNRs decreased from 1,265 m^2/g for CMSNRs1 to 580 m^2/g for CMSNRs4 (Fig. 2(c)).

It has been reported that nonspherical nanoparticles may show advantages in cellular uptake compared to spherical nanoparticles [42, 43]. To understand whether the morphology of CMSNRs played a role in their interactions with cells, we incubated CMSNRs1–4 (which have varying aspect ratios) at the same Si concentration with 4T1 cancer cells for different periods of time. After removal of free nanoparticles, cells were lyzed and solubilized to determine the amounts of Si inside cells by ICP–AES (Fig. 3(a)). As

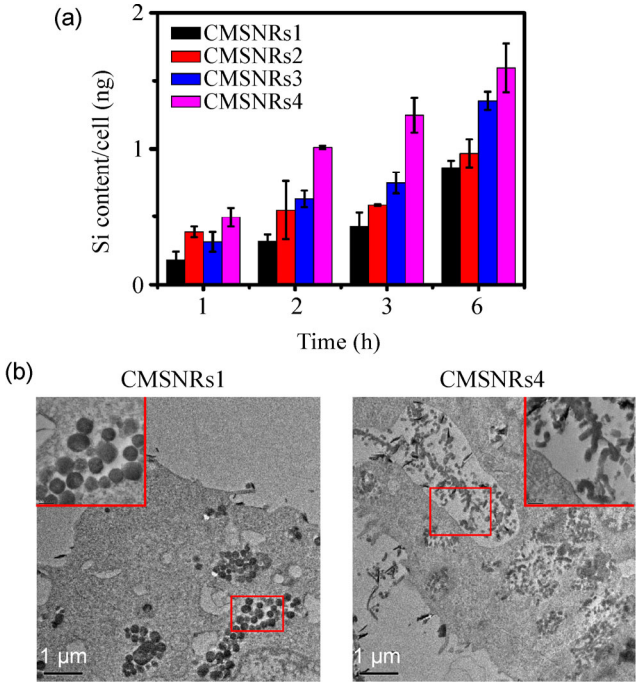

Figure 3 Cellular uptake of CMSNRs. (a) ICP-AES measured Si content per cell for 4T1 cells after incubation with CMSNRs1–4 at the same silica concentration for different periods of time. The background Si content per cell has been subtracted from those data. CMSNRs with higher aspect ratios showed enhanced cellular uptake. (b) TEM images of 4T1 cells incubated with CMSNRs1 and CMSNRs4 for 6 h. Large numbers of nanoparticles were found inside those cells.

aspect ratio increased from CMSNR1 to CMSNR4, the Si level inside cells showed an obvious increase, suggesting that the cellular uptake of nanoparticles was shape-dependent, and rod-like nanoparticles with higher aspect ratios showed enhanced cellular uptake compared with spherical nanoparticles. TEM images of cell slices revealed that CMSNRs1 and CMSNRs4 still displayed intact morphologies after cell uptake (Fig. 3(b)). Considering the fact that CMSNRs were not able to enter cells below 4 ℃, as well as the co-localization of CMSNRs signals with lyso-tracker signals under the confocal microscope, the cellular uptake mechanism for CMSNRs is most likely be via the energy-dependent endocytosis pathway (Fig. S3, in the ESM).

We next studied the drug loading ability of CMSNRs using DOX, a widely used anti-cancer drug, as a model drug molecule. Four types of CMSNRs at the concentration of 2 mg/mL were mixed with different concentrations of DOX in phosphate buffer (PB) at pH 8.0 overnight in the dark. Excess DOX molecules were removed by centrifugation at 14,800 rpm for 5 min and washing with several times water. The UV–Vis absorption spectra of CMSNRs/DOX were then recorded (Fig. 4(b)). Based on the characteristic DOX absorbance peak at 490 nm, the drug loading capacities on CMSNRs were determined. The DOX loading capacity increased with increasing DOX concentrations and reached a maximum for a DOX concentration of 0.188 mg/mL (Fig. 4(c)). Above this concentration the complexes became unstable in aqueous solution. Notably, the four types of CMSNRs showed similar maximal DOX loading capacities (Fig. S4, in the ESM), despite the smaller BET-measured specific surface area of CMSNRs4. We therefore chose CMSNRs4/DOX with the highest Ce6 loading, faster uptake by cancer cells, and similar DOX loading compared with other CMSNRs for the following experiments.

The generation of singlet oxygen (SO) by nanoparticles was detected using the singlet oxygen sensor green (SOSG) as the probe molecule, whose quenched fluorescence in aqueous solution is recovered in the presence of SO [44, 45]. The fluorescence intensity of SOSG in the CMSNRs4/DOX sample exhibited a time-dependent enhancement upon irradiation with 660-nm light, suggesting the effective SO production by CMSNRs4 under light exposure (Fig. 4(d)). However, compared with free Ce6, CMSNRs4 and CMSNRs4/DOX at the same Ce6 concentration showed slightly lowered SO production efficiency. This is likely due to the less effective interaction between oxygen and Ce6 molecules doped inside the silica nanostructure (Fig. 4(e)). Nevertheless, the light-induced SO generation by CMSNRs4/DOX remained at a significant level that could allow us to use it as a photodynamic agent.

In our multifunctional CMSNRs4/DOX nanosystem, photodynamic therapy can be achieved without the need of Ce6 release, while chemotherapeutic effect of DOX becomes effective only after DOX is released from the nanocarriers and enters cell nuclei. The drug release behavior of CMSNRs4/DOX was thus determined by incubating CMSNRs4/DOX in phosphate buffers at different pH (7.4 and 5.5) and measuring the concentrations of released Ce6 and DOX at various time intervals (Figs. 4(f) and 4(g)). While the Ce6 loading in CMSNRs via covalent conjugation was rather stable in both neutral and acidic pHs, DOX non-covalently adsorbed into the mesoporous structure of CMSNRs showed a much faster, pH-dependent release kinetics. At physiological pH (7.4), approximately 28% of DOX was released from CMSNRs4/DOX within 24 h, in marked contrast to the ~70% of DOX released at pH 5.5. Protonation of amino group in the DOX molecule is likely the reason that results in the acid-triggered drug release behavior, which is preferred for anti-cancer drug delivery systems as the tumor microenvironment and the cell endosomes/lysosomes are slightly acidic.

In order to study the intracellular delivery behavior of our multifunctional drug delivery system, 4T1 murine breast cancer cells were incubated with CMSNRs4/DOX for different periods of time and imaged under a confocal fluorescence microscope (Fig. 5(a)). Both Ce6 and DOX fluorescence inside cells increased with prolonging of the incubation time. Importantly, while Ce6 fluorescence remained in the cytoplasm of cells without nuclei entry even after 10 h of incubation, significant accumulation of DOX inside cell nuclei was observed at later time points. Those results indicate the gradual intracellular

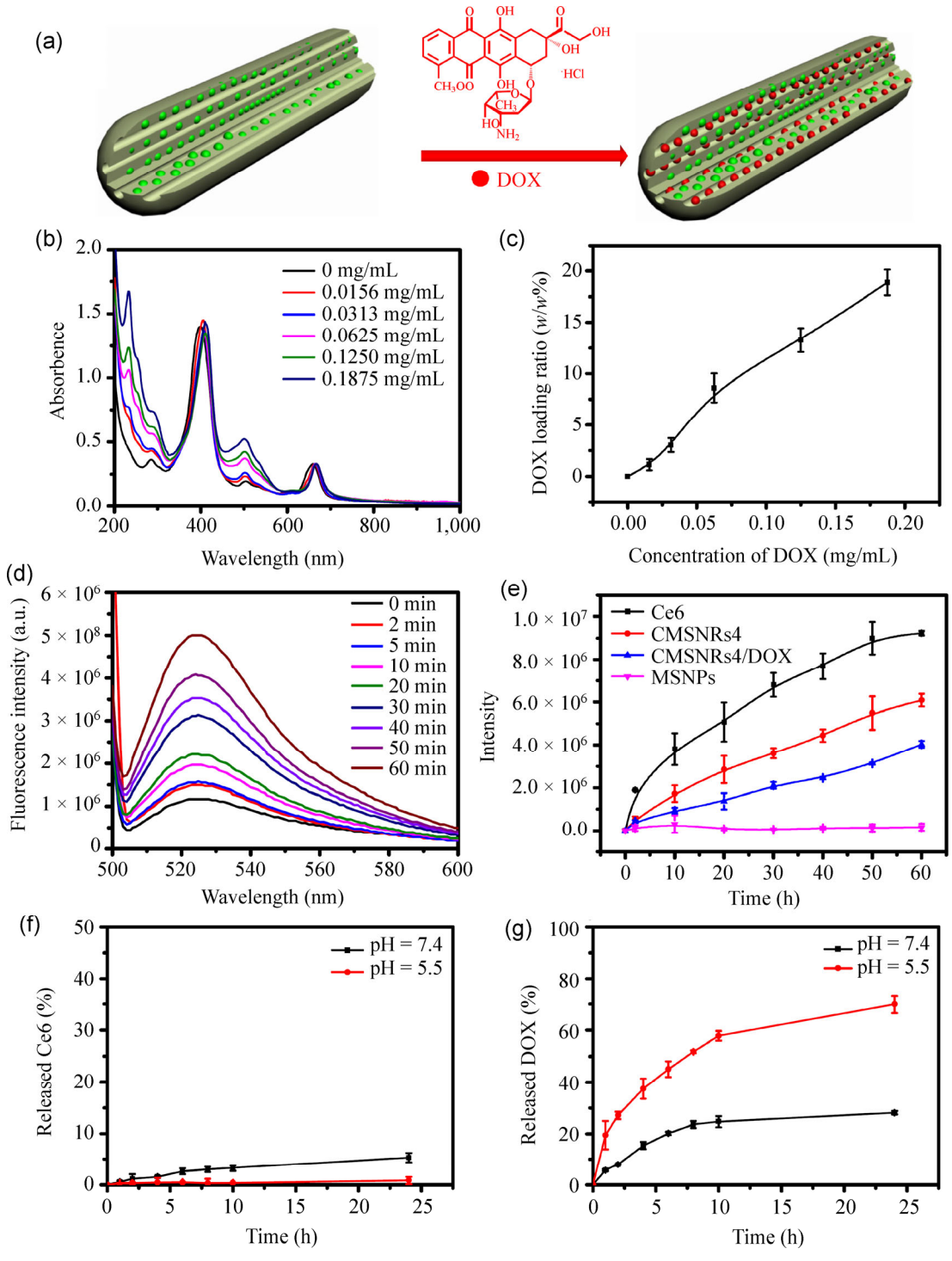

Figure 4 (a) Schematic illustration of the loading of DOX into CMSNRs. (b) UV–Vis absorbance spectra of CMSNRs4 loaded with different concentrations of DOX. (c) Quantification of DOX loading at different feeding DOX concentrations. (d) Fluorescence emission spectra of SOSG in the CMSNRs4 solution with the increase of light irradiation time (660 nm, 5 mW/cm^2). (e) The changes of SOSG fluorescence intensity as a function of light irradiation time for different samples including Ce6, CMSNRs4, and CMSNRs4/DOX at the same Ce6 concentration (0.2 μM). MSNPs solution without Ce6 doping was used as the control. Percentages of released Ce6 (f) and DOX (g) from CMSNRs4/DOX over time in buffers at the two different pH values.

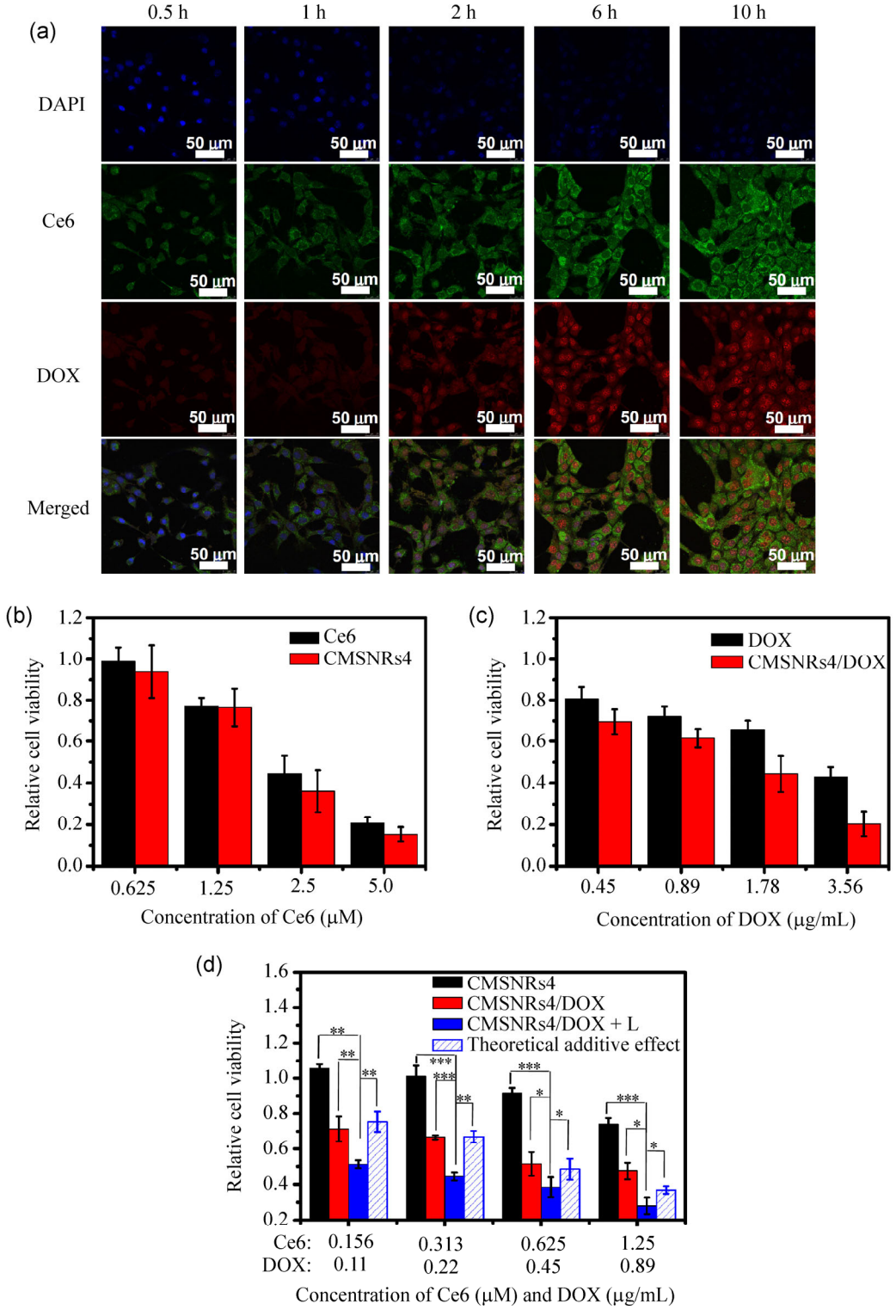

Figure 5 Cellular uptake and *in vitro* combination therapy. (a) Confocal images of 4T1 cells incubated with CMSNRs4/DOX at different times points. Green, red, and blue represent Ce6, DOX, and DAPI fluorescence, respectively. (b) Relative viabilities of 4T1 cells after incubation with different concentrations of Ce6 and CMSNR4 under 660-nm light irradiation (5 mW/cm^2, 1 h). (c) Relative viabilities of 4T1 cells after incubation with various concentrations of free DOX and CMSNRs4/DOX in dark. (d) Relative viabilities of 4T1 cells after treated with CMSNRs4 plus light, CMSNRs4/DOX in dark, and CMSNRs4/DOX plus light (660 nm, 5 mW/cm^2, and 1 h). *P* values were calculated by Tukey's post-test (***$p < 0.001$, **$p < 0.01$, or *$p < 0.05$).

release of DOX from CMSNRs4 nanocarriers, which mainly locate inside cell endosomes and lysosomes after endocytosis.

Before determining the therapeutic efficiency of CMSNRs4/DOX in cell experiments, we first tested the cytotoxicity of CMSNRs4 in the dark. Cell viability tests based on the standard methyl thiazolyl tetrazolium MTT (Sigma Inc.) assay showed that CMSNRs4 exhibited no obvious dark toxicity to different types of cells (4T1, 293T, Hela) even at high concentrations of nanoparticles up to 125 μg/mL (Fig. S5, in the ESM). The *in vitro* efficacies of photodynamic therapy, chemotherapy and combination therapy were then evaluated with 4T1 cells. Under 660-nm light exposure (5 mW/cm^2 for 1 h), the cancer cell killing efficiency of CMSNRs4 was found to be comparable or slightly stronger than that of free Ce6 (Fig. 5(b)), likely owing to the enhanced cellular uptake of Ce6 in our nanorod formulation (Fig. S6, in the ESM). As for chemotherapy, CMSNRs4/DOX appeared to be obviously more toxic to cancer cells than free DOX at our tested concentrations (Fig. 5(c)). The combined PDT and chemotherapy was then studied by treating cells with CMSNRs4 + light, CMSNRs4/DOX in the dark, and CMSNRs4/DOX + light. The last group of cells after combination therapy showed the lowest remaining cell viabilities compared those after different monotherapies were conducted (Fig. 5(d)). The theoretical additive effects were calculated and presented in Fig. 5(d). Remarkably, the therapeutic effects of combination therapy achieved in our experiments appeared to be obviously higher than that of the simple additive effect, suggesting that the combined PDT + chemotherapy delivered by CMSNRs4/DOX resulted in a synergistic effect in killing cancer cells.

Finally, we ought to demonstrate the combination therapy with CMSNRs4/DOX in animal experiments. A total of 30 Balb/c mice bearing 4T1 tumors were divided into six groups with five mice per group: Untreated (Group 1), Ce6 + DOX + 660-nm light (Group 2), CMSNRs4 (Group 3), CMSNRs4 + 660-nm light (Group 4), CMSNRs4/DOX (Group 5), CMSNRs4/DOX + 660-nm light (Group 6). The therapeutic agents with the same equivalent Ce6 and DOX concentrations (Ce6: 0.4 mg/mL, DOX: 1 mg/mL) at the volume of 50 μL were intratumorally (i.t.) injected into those mice. For PDT treatment, tumors were exposed to 660-nm light for 1 h at the power density of 5 mW/cm^2 to induce SO production.

The tumor sizes and mouse body weights were measured every the other day (Figs. 6(a) and 6(c)) over two weeks. At day 14, tumors from all groups of mice were collected and weighed (Fig. 6(b)). Mice receiving CMSNRs4/DOX with light treatment exhibited the smallest tumor volumes, with their tumor growth inhibited by ~60%. For the other groups, the tumor growth inhibition effects were determined to be 42%, 12%, and 27%, for Ce6 + DOX (light), CMSNRs4 (light), CMSNRs4/DOX (light) groups, respectively. Notably, the therapeutic efficacy achieved in our combination therapy appeared to be obviously stronger than the simple theoretical addictive effect (Fig. 6(b)). These results demonstrated the synergistic effect of combined PDT/chemotherapy over different monotherapies conducted separately. In addition, compared with combination therapy using free drugs (Ce6 + DOX), the nanoparticle formulation had longer retention times in the tumor and thus offered improved therapeutic outcomes.

In our experiments, animals after various treatments showed no obvious body weight drop (Fig. 6(c)). Histology examination by hematoxylin and eosin (H&E) staining was carried by harvesting major organs and tumors from untreated mice and CMSNRs4/DOX treated mice (with light exposure) (Fig. 6(d)). No apparent toxicity or abnormality was observed for all examined major organs including liver, spleen, kidney, heart and lung, indicating that combination therapy induced by those nanoparticles resulted in no significant short-term side effects to the animals. On the other hand, H&E staining of tumor slices showed that while cells in untreated tumors largely retained their normal morphology with distinctive membrane and nuclear structures, tumor cells in the treatment group (CMSNRs4/DOX + light irradiation) were severely damaged (Fig. 6(d)). These results were in good agreement with the tumor growth data, further confirming the therapeutic efficacy achieved by combination therapy with CMSNRs4/DOX.

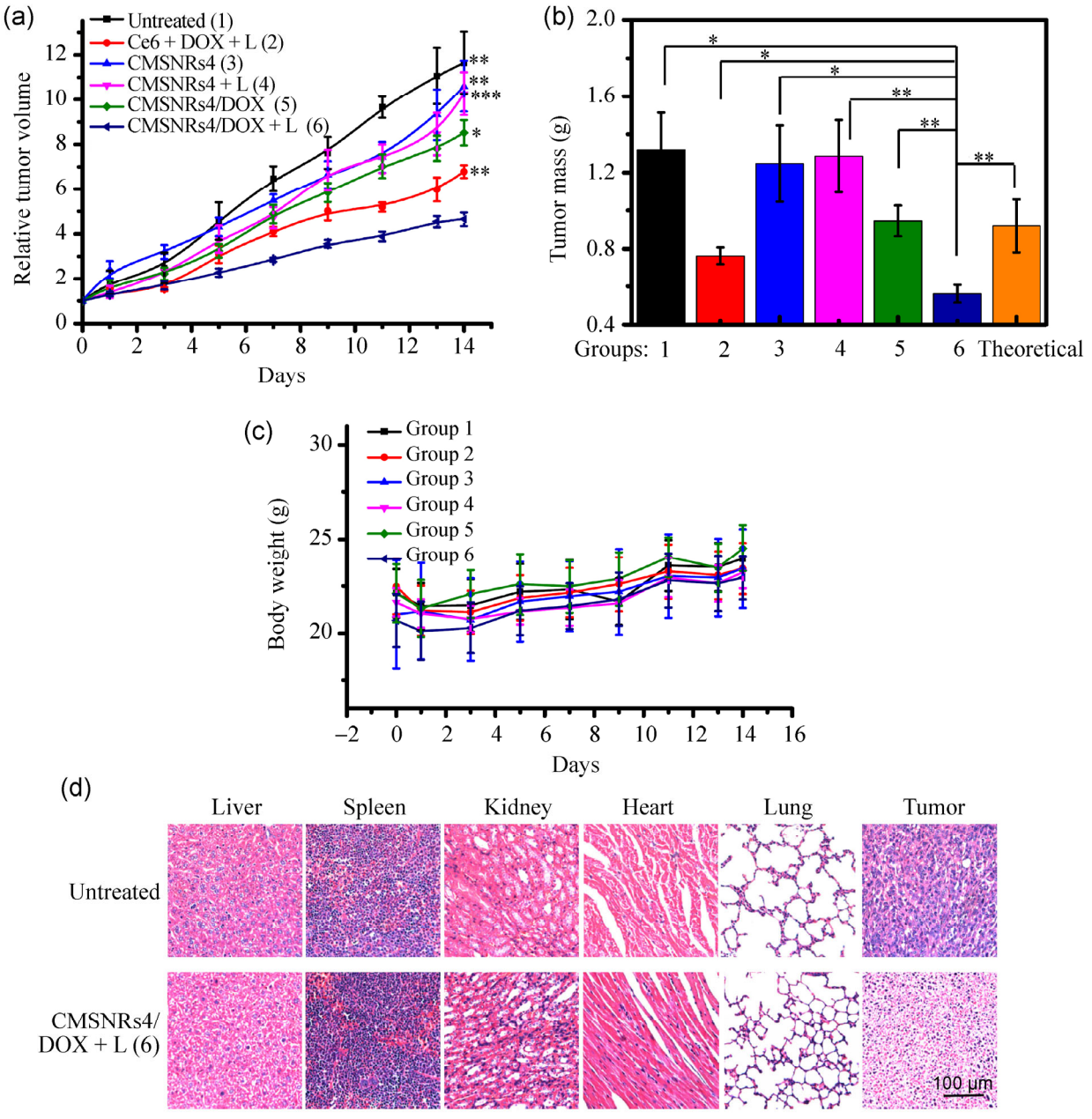

Figure 6 MSNRs4/DOX for *in vivo* combination therapy. (a) Tumor growth curves of different groups of mice after various treatments indicated (five mice per group). Error bars were based on standard errors of the mean (SEM). (b) Average weights of tumors collected from mice at the end of various treatments indicated. Error bars are based on SEM. (c) Average body weights of mice after various treatments indicated. (d) H&E stained images of major organs and tumor slices collected from untreated mice and mice after CMSNRs4/DOX-based combination therapy at day 7 post treatment. *P* values in (a) and (b) were calculated by Tukey's post-test (***$p < 0.001$, **$p < 0.01$, or *$p < 0.05$).

4 Conclusion

We have fabricated a new class of mesoporous silica nanostructures with multiple functions for combination therapy of cancer. In our system, by covalently doping Ce6, a photodynamic agent, into the silica matrix, mesoporous silica nanorods with controllable aspect ratios can be synthesized. CMSNRs4 with the largest aspect ratio, highest Ce6 loading, and fastest uptake by cancer cells, was then chosen as the drug

delivery platform. Utilizing DOX-loaded CMSNRs4, combined PDT and chemotherapy of cancer was successfully realized in both *in vitro* cellular experiments and *in vivo* animal studies. The therapeutic efficacy achieved by such a combination therapy appears to be the result of an obvious synergistic effect rather than simply the additive effect of two monotherapies. Further studies are still ongoing in our laboratory aiming at achieving imaging-guided tumor combination therapy using such MSN-based theranostic systems after systemic administration. Nevertheless, our study presents an interesting approach to fabricate silica nanostructures with well-controlled morphologies by doping organic molecules into the silica matrix. Such a strategy may be extended to other types of functional molecules to develop novel types of MSNs as theranostic platforms. Compared with other MSN-based multifunctional nanoparticles—which usually involve complicated structures and surface engineering—our Ce6-doped MSNRs, which can be easily fabricated and show rather simple structure, are a promising type of platform for combination therapy of cancer.

Acknowledgements

This work was partially supported by the National Basic Research Programs of China (973 Program) (Nos. 2012CB932600 and 2011CB911002), the National Natural Science Foundation of China (Nos. 51222203 and 51132006), Jiangsu Key Laboratory for Carbon-Based Functional Materials and Devices, a Jiangsu Natural Science Fund for Distinguished Young Scholars, and a Project Funded by the Priority Academic Program Development (PAPD) of Jiangsu Higher Education Institutions.

Electronic Supplementary Material: Supplementary material (TEM images of CMSNRs, photograph of the nanoparticle and UV–Vis absorbance spectra, quantitative flow cytometry data and confocal images, UV–Vis absorbance spectra of CMSNRs1-CMSNRs4 loaded with DOX, relative viabilities of 4T1, Hela, and 293T cells after being incubated with CMSNRs4) is available in the online version of this article at http://dx.doi.org/10.1007/s12274-014-0558-0.

References

[1] Tang, F. Q.; Li, L. L.; Chen, D. Mesoporous silica nanoparticles: Synthesis, biocompatibility and drug delivery. *Adv. Mater.* **2012**, *24*, 1504–1534.

[2] Chen, Y.; Chen, H. R.; Shi, J. L. *In vivo* bio-safety evaluations and diagnostic/therapeutic applications of chemically designed mesoporous silica nanoparticles. *Adv. Mater.* **2013**, *25*, 3144–3176.

[3] Yang, J. P.; Shen, D. K.; Zhou, L.; Li, W.; Li, X. M.; Yao, C.; Wang, R.; El-Toni, A. M.; Zhang, F.; Zhao, D. Y. Spatially confined fabrication of core–shell gold nanocages@ mesoporous silica for near-infrared controlled photothermal drug release. *Chem. Mater.* **2013**, *25*, 3030–3037.

[4] Zhang, F.; Braun, G. B.; Pallaoro, A.; Zhang, Y. C.; Shi, Y. F.; Cui, D. X.; Moskovits, M.; Zhao, D. Y.; Stucky, G. D. Mesoporous multifunctional upconversion luminescent and magnetic "nanorattle" materials for targeted chemotherapy. *Nano Lett.* **2011**, *12*, 61–67.

[5] Luo, Z.; Hu, Y.; Xin, R. L.; Zhang, B. L.; Li, J. H.; Ding, X. W.; Hou, Y. H.; Yang, L.; Cai, K. Y. Surface functionalized mesoporous silica nanoparticles with natural proteins for reduced immunotoxicity. *J. Biomed. Mater. Res. A* **2013**, in press, DOI: 10.1002/jbm.a.35049.

[6] Xie, J.; Lee, S.; Chen, X. Y. Nanoparticle-based theranostic agents. *Adv. Drug Delivery Rev.* **2010**, *62*, 1064–1079.

[7] Wang, L.; Zhao, W. J.; Tan, W. H. Bioconjugated silica nanoparticles: Development and applications. *Nano Res.* **2008**, *1*, 99–115.

[8] Estévez, M. C.; O'Donoghue, M. B.;Chen, X. L.; Tan, W. L. Highly fluorescent dye-doped silica nanoparticles increase flow cytometry sensitivity for cancer cell monitoring. *Nano Res.* **2009**, *2*, 448–461.

[9] Huang, C. M.; Cheng, S. H.; Jeng, U. S.; Yang, C. S.; Lo, L. W. Formation of CdSe/CdS/ZnS–Au/SiO_2 dual–yolk/shell nanostructures through a Trojan-type inside–out etching strategy. *Nano Res.* **2012**, *5*, 654–666.

[10] Zhang, Q.; Ge, J. P.; Goebl, J.; Hu, Y. X.; Lu, Z. D.; Yin, Y. D. Rattle-type silica colloidal particles prepared by a surface-protected etching process. *Nano Res.* **2009**, *2*, 583–591.

[11] Qian, R. C.; Ding, L.; Ju, H. X. Switchable fluorescent imaging of intracellular telomerase activity using telomerase-responsive mesoporous silica nanoparticle. *J. Am. Chem. Soc.* **2013**, *135*, 13282–13285.

[12] Sreejith, S.; Ma, X.; Zhao, Y. L. Graphene oxide wrapping on squaraine-loaded mesoporous silica nanoparticles for bioimaging. *J. Am. Chem. Soc.* **2012**, *134*, 17346–17349.

[13] Fan, W. P.; Shen, B.; Bu, W. B.; Chen, F.; Zhao, K. L.; Zhang, S. J.; Zhou, L. P.; Peng, W. J.; Xiao, Q. F.; Xing, H. Y. et al. Rattle-structured multifunctional nanotheranostics for synergetic chemo-/radiotherapy and simultaneous magnetic/luminescent dual-mode imaging. *J. Am. Chem. Soc.* **2013**, *135*, 6494–6503.

[14] Chen, F.; Hong, H.; Zhang, Y.; Valdovinos, H. F.; Shi, S. X.; Kwon, G. S.; Theuer, C. P.; Barnhart, T. E.; Cai, W. B. *In vivo* tumor targeting and image-guided drug delivery with antibody-conjugated, radiolabeled mesoporous silica nanoparticles. *ACS Nano* **2013**, *7*, 9027–9039.

[15] Shi, S. X.; Chen, F.; Cai, W. B. Biomedical applications of functionalized hollow mesoporous silica nanoparticles: Focusing on molecular imaging. *Nanomedicine* **2013**, *8*, 2027–2039.

[16] Fang, W. J.; Yang, J.; Gong, J. W.; Zheng, N. F. Photo- and pH-triggered release of anticancer drugs from mesoporous silica-coated Pd@Ag nanoparticles. *Adv. Funct. Mater.* **2012**, *22*, 842–848.

[17] Gao, Y.; Chen, Y.; Ji, X. F.; He, X. Y.; Yin, Q.; Zhang, Z. W.; Shi, J. L.; Li, Y. P. Controlled intracellular release of doxorubicin in multidrug-resistant cancer cells by tuning the shell–pore sizes of mesoporous silica nanoparticles. *ACS Nano* **2011**, *5*, 9788–9798.

[18] Lee, C. H.; Cheng, S. H.; Huang, I. P.; Souris, J. S.; Yang, C. S.; Mou, C. Y.; Lo, L. W. Intracellular pH-responsive mesoporous silica nanoparticles for the controlled release of anticancer chemotherapeutics. *Angew. Chem. Int. Ed.* **2010**, *49*, 8214–8219.

[19] Zhao, Y.; Lin, L. N.; Lu, Y.; Chen, S. F.; Dong, L.; Yu, S. H. Templating synthesis of preloaded doxorubicin in hollow mesoporous silica nanospheres for biomedical applications. *Adv. Mater.* **2010**, *22*, 5255–5259.

[20] Ma, X.; Sreejith, S.; Zhao, Y. L. Spacer intercalated disassembly and photodynamic activity of zinc phthalocyanine inside nanochannels of mesoporous silica nanoparticles. *ACS Appl. Mater. Interfaces* **2013**, *5*, 12860–12868.

[21] Luo, Z.; Cai, K. Y.; Hu, Y.; Zhao, L.; Liu, P.; Duan, L.; Yang, W. H. Mesoporous silica nanoparticles end-capped with collagen: Redox-responsive nanoreservoirs for targeted drug delivery. *Angew. Chem. Int. Ed.* **2011**, *50*, 640–643.

[22] Kim, M. H.; Na, H. K.; Kim, Y. K.; Ryoo, S. R.; Cho, H. S.; Lee, K. E.; Jeon, H.; Ryoo, R.; Min, D. H. Facile synthesis of monodispersed mesoporous silica nanoparticles with ultralarge pores and their application in gene delivery. *ACS Nano* **2011**, *5*, 3568–3576.

[23] Suwalski, A.; Dabboue, H.; Delalande, A.; Bensamoun, S. F.; Canon, F.; Midoux, P.; Saillant, G.; Klatzmann, D.; Salvetat, J. P.; Pichon, C. Accelerated achilles tendon healing by PDGF gene delivery with mesoporous silica nanoparticles. *Biomaterials* **2010**, *31*, 5237–5245.

[24] Li, Z. W.; Wang, C.; Cheng, L.; Gong, H.; Yin, S. N.; Gong, Q. F.; Li, Y. G.; Liu, Z. PEG-functionalized iron oxide nanoclusters loaded with chlorin e6 for targeted, NIR light induced, photodynamic therapy. *Biomaterials* **2013**, *34*, 9160–9170.

[25] Wang, C.; Tao, H. Q.; Cheng, L.; Liu, Z. Near-infrared light induced *in vivo* photodynamic therapy of cancer based on upconversion nanoparticles. *Biomaterials* **2011**, *32*, 6145–6154.

[26] Cakmak, Y.; Kolemen, S.; Duman, S.; Dede, Y.; Dolen, Y.; Kilic, B.; Kostereli, Z.; Yildirim, L. T.; Dogan, A. L.; Guc, D. et al. Designing excited states: Theory-guided access to efficient photosensitizers for photodynamic action. *Angew. Chem. Int. Ed.* **2011**, *50*, 11937–11941.

[27] Park, S. Y.; Baik, H. J.; Oh, Y. T.; Oh, K. T.; Youn, Y. S.; Lee, E. S. A smart polysaccharide/drug conjugate for photodynamic therapy. *Angew. Chem. Int. Ed.* **2011**, *50*, 1644–1647.

[28] Huang, P.; Lin, J.; Wang, S. J.; Zhou, Z. J.; Li, Z. M.; Wang, Z.; Zhang, C. L.; Yue, X. Y.; Niu, G.; Yang, M. et al. Photosensitizer-conjugated silica-coated gold nanoclusters for fluorescence imaging-guided photodynamic therapy. *Biomaterials* **2013**, *34*, 4643–4654.

[29] Celli, J. P.; Spring, B. Q.; Rizvi, I.; Evans, C. L.; Samkoe, K. S.; Verma, S.; Pogue, B. W.; Hasan, T. Imaging and photodynamic therapy: Mechanisms, monitoring, and optimization. *Chem. Rev.* **2010**, *110*, 2795–2838.

[30] Meng, H.; Liong, M.; Xia, T.; Li, Z. X.; Ji, Z. X.; Zink, J. I.; Nel, A. E. Engineered design of mesoporous silica nanoparticles to deliver doxorubicin and P-glycoprotein siRNA to overcome drug resistance in a cancer cell line. *ACS Nano* **2010**, *4*, 4539–4550.

[31] Chen, Y. W.; Chen, P. J.; Hu, S. H.; Chen, I. W.; Chen, S. Y. NIR-triggered synergic photo-chemothermal therapy delivered by reduced graphene oxide/carbon/mesoporous silica nanocookies. *Adv. Funct. Mater.* **2014**, *24*, 451–459.

[32] Couleaud, P.; Morosini, V.; Frochot, C.; Richeter, S.; Raehm, L.; Durand, J. O. Silica-based nanoparticles for photodynamic therapy applications. *Nanoscale* **2010**, *2*, 1083–1095.

[33] Wang, T. T.; Zhang, L. Y.; Su, Z. M.; Wang, C. G.; Liao, Y.; Fu, Q. Multifunctional hollow mesoporous silica nanocages for cancer cell detection and the combined chemotherapy and photodynamic therapy. *ACS Appl. Mater. Interfaces* **2011**, *3*, 2479–2486.

[34] He, Q. J.; Shi, J. L. MSN anti-cancer nanomedicines: Chemotherapy enhancement, overcoming of drug resistance,

and metastasis inhibition. *Adv. Mater.* **2014**, *26*, 391–411.

[35] Lee, J.; Park, J.; Singha, K.; Kim, W. J. Mesoporous silica nanoparticle facilitated drug release through cascade photosensitizer activation and cleavage of singlet oxygen sensitive linker. *Chem. Commun.* **2013**, *49*, 1545–1547.

[36] Hayashi, K.; Nakamura, M.; Ishimura, K. Silica–porphyrin hybrid nanotubes for *in vivo* cell tracking by near-infrared fluorescence imaging. *Chem. Commun.* **2012**, *48*, 3830–3832.

[37] Hayashi, K.; Nakamura, M.; Miki, H.; Ozaki, S.; Abe, M.; Matsumoto, T.; Ishimura, K. Near-infrared fluorescent silica/porphyrin hybrid nanorings for *in vivo* cancer imaging. *Adv. Funct. Mater.* **2012**, *22*, 3539–3546.

[38] Rossi, L. M.; Silva, P. R.; Vono, L. L. R.;Fernandes, A. U.; Tada, D. B.; Baptista, M. S. Protoporphyrin IX nanoparticle carrier: Preparation, optical properties, and singlet oxygen generation. *Langmuir* **2008**, *24*, 12534–12538.

[39] Cheng, S. H.; Lee, C. H.; Yang, C. S.; Tseng, F. G.; Mou, C. Y.; Lo, L. W. Mesoporous silica nanoparticles functionalized with an oxygen-sensing probe for cell photodynamic therapy: Potential cancer theranostics. *J. Mater. Chem.* **2009**, *19*, 1252–1257.

[40] Tu, H. L.; Lin, Y. S.; Lin, H. Y.; Hung, Y.; Lo, L. W.; Chen, Y. F.; Mou, C. Y. *In vitro* studies of functionalized mesoporous silica nanoparticles for photodynamic therapy. *Adv. Mater.* **2009**, *21*, 172–177.

[41] Zhang, R. R.; Wu, C. L.; Tong, L. L.; Tang, B.; Xu, Q. H. Multifunctional core–shell nanoparticles as highly efficient imaging and photosensitizing agents. *Langmuir* **2009**, *25*, 10153–10158.

[42] Meng, H.; Yang, S.; Li, Z. X.; Xia, T.; Chen, J.; Ji, Z. X.; Zhang, H. Y.; Wang, X.; Lin, S. J.; Huang, C. et al. Aspect ratio determines the quantity of mesoporous silica nanoparticle uptake by a small GTPase-dependent macropinocytosis mechanism. *ACS Nano* **2011**, *5*, 4434–4447.

[43] Huang, X. L.; Teng, X.; Chen, D.; Tang, F. Q.; He, J. Q. The effect of the shape of mesoporous silica nanoparticles on cellular uptake and cell function. *Biomaterials* **2010**, *31*, 438–448.

[44] Hassan, M.; Klaunberg, B. A. Biomedical applications of fluorescence imaging *in vivo*. *Comparative Med.* **2004**, *54*, 635–644.

[45] Zhu, Z.; Tang, Z. W.; Phillips, J. A.; Yang, R. H.; Wang, H.; Tan, W. H. Regulation of singlet oxygen generation using single-walled carbon nanotubes. *J. Am. Chem. Soc.* **2008**, *130*, 10856–10857.